Int. J. Solids Structures Vol. 29, No. 5, pp. 571–589, 1992
Printed in Great Britain.

0020-7683/92 $5.00 + .00

TEST GEOMETRIES FOR MEASURING INTERFACIAL FRACTURE TOUGHNESS

N. P. O'DOWD,† C. F. SHIH† and M. G. STOUT‡
† Division of Engineering, Brown University, Providence, RI 02912, U.S.A.
‡ Physical Metallurgy Group, Los Alamos National Laboratories, Los Alamos, NM 87545, U.S.A.

(*Received* 19 *November* 1990; *in revised form* 8 *April* 1991)

Abstract—Two types of test specimen for determining interfacial fracture toughness are calibrated in this paper. Previous studies have shown that interfacial fracture toughness is strongly dependent on mode mixity. Both specimen types presented are well-suited for investigating interfacial toughness over a wide range of mode mixities. The structure of the near tip elastic fields for an interface crack is examined and in particular near tip contact and the variation of mode mixity with distance are dealt with. The concept of K dominance for interface cracks is discussed and a zone of K dominance is shown to exist for the specimens calibrated, provided the zone of non-linear effects is small. A procedure for determining the effect of residual stresses on the stress intensity factor is presented.

1. INTRODUCTION

A number of test specimens for investigating interfacial fracture toughness have been developed recently (e.g. Suo and Hutchinson, 1989; Cao and Evans, 1989; Charalambides *et al.*, 1989; Wang and Suo, 1990). For these specimens a thin layer of material is sandwiched between two layers of a second material. This type of specimen can be calibrated in terms of the stress intensity factor for a homogeneous specimen of the bulk material. The specimens presented in this paper consist of two slabs of dissimilar material bonded together with a crack lying on the interface of the two materials. Two types of specimen are calibrated: a Brazilian disk specimen and a bend bar type geometry. The latter geometry is calibrated for a three-point and four-point bend configuration. The four-point bend specimen is a development of an earlier specimen used for measuring mixed mode fracture toughness in homogeneous materials (Suresh *et al.*, 1990). The four-point bend specimen and Brazilian disk are currently being used to investigate the fracture toughness of a niobium/alumina interface (Stout *et al.*, unpublished).

A crack in an isotropic, homogeneous material tends to grown in opening mode, and hence fracture toughness is characterized by a single parameter, Mode I toughness, K_{IC}. However, a crack lying on an interface often tends to grow along the interface. Since the crack grows under mixed mode conditions it is necessary to quantify interfacial fracture toughness as a function of mode mixity. The specimens presented here allow us to vary the mode mixity systematically and thus fracture toughness can be measured for the full range of mode mixities.

Results for a number of bimaterial systems are presented and attention is restricted to plane stress and plane strain.

2. SPECIMEN GEOMETRY

The test specimens to be calibrated are shown in Fig. 1. The symmetric four-point bend and three-point bend specimens, shown in Fig. 1a, c are tension-dominated geometries giving rise to pure Mode I conditions at the crack tip for a homogeneous specimen. The asymmetric four-point bend specimen, shown in Fig. 1b, has been used to measure fracture toughness in a homogeneous material (Suresh *et al.*, 1990). For a homogeneous material pure Mode II conditions are obtained with load offset, $s = 0$ (provided $A \neq B$). Increasing the load offset increases the local Mode I contribution. Figure 1d shows the Brazilian disk specimen. The mode mixity is varied by changing the compression angle θ, which can range from $-\pi/2$ to $\pi/2$. The calibration functions for a homogeneous Brazilian disk can be found

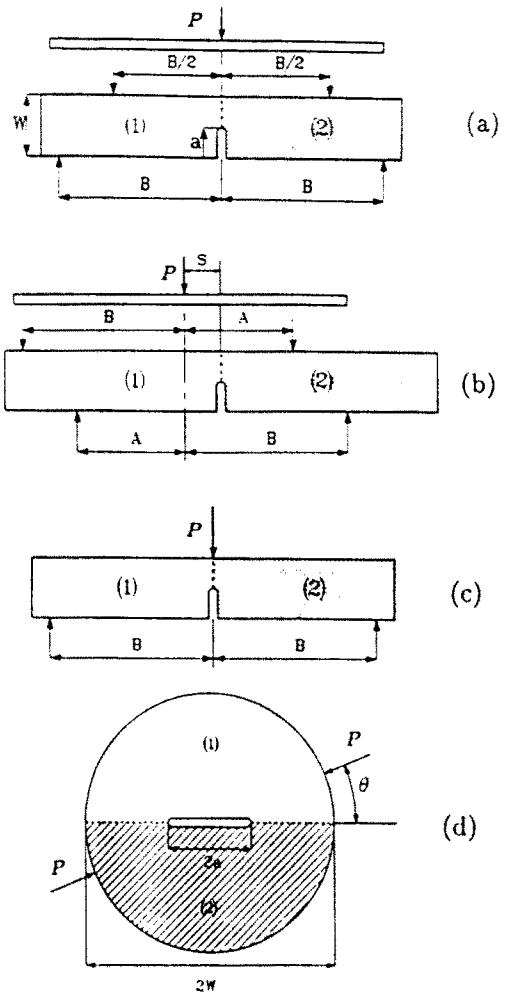

Fig. 1. Test specimens. (a) Symmetric four-point bend bar, (b) asymmetric four-point bend bar, (c) three-point bend bar, (d) Brazilian disk.

in Atkinson *et al.* (1982). For a homogeneous material pure Mode I conditions are achieved when $\theta = 0$ and pure Mode II conditions when $\theta \approx 25^\circ$. Shetty *et al.* (1987) have used the Brazilian disk to study the mixed mode fracture toughness of soda-lime glass. Wang and Suo (1990) have measured interfacial fracture toughness for epoxy/metal and epoxy/ceramic systems using a Brazilian disk sandwich.

For the bend bar the material to the left of the crack is designated material 1 and the material to the right is material 2. For the Brazilian disk the upper material is material 1 and the lower material is material 2.

3. INTERFACIAL FRACTURE MECHANICS

3.1. *Elastic crack tip fields*

We consider a crack lying on an interface separating two isotropic elastic materials as shown in Fig. 2. The standard notation for interface cracks is used throughout. The asymptotic solution for the in-plane stresses is

$$\sigma_{ij} = \frac{1}{\sqrt{2\pi r}}[\mathrm{Re}\{Kr^{i\varepsilon}\}\tilde{\sigma}_{ij}^{I}(\theta;\varepsilon) + \mathrm{Im}\{Kr^{i\varepsilon}\}\tilde{\sigma}_{ij}^{II}(\theta;\varepsilon)]. \tag{1}$$

ε is the bimaterial constant given by

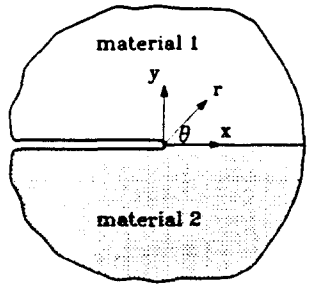

Fig. 2. Crack lying on bimaterial interface.

$$\varepsilon = \frac{1}{2\pi} \ln \left\{ \frac{\kappa_1/\mu_1 + 1/\mu_2}{\kappa_2/\mu_2 + 1/\mu_1} \right\} \tag{2}$$

where $\kappa = 3-4\nu$ for plane strain, $\kappa = (3-\nu)/(1+\nu)$ for plane stress, ν is Poisson's ratio, and μ the shear modulus. The subscripts 1 and 2 refer to the upper and lower material, respectively. The dimensionless angular functions $\tilde{\sigma}_{ij}^{I}$ and $\tilde{\sigma}_{ij}^{II}$ are given in Rice *et al.* (1990). The functions are scaled so that the tractions ahead of the crack are given by:

$$t = |t| e^{i\psi_r} = (\sigma_{yy} + i\sigma_{xy})_{\theta=0} = \frac{Kr^{i\varepsilon}}{\sqrt{2\pi r}}. \tag{3}$$

ψ_r is the phase angle or mode mixity at distance r and gives the ratio of the normal to shear stress ahead of the crack.

The complex stress intensity factor K in (1) and (3) has the generic form

$$K = YT\sqrt{L} L^{-i\varepsilon} e^{i\psi}. \tag{4}$$

L is a characteristic dimension of the crack geometry which for the specimens discussed here is taken to be the crack length. T is a representative stress amplitude. By definition ψ is the phase of $KL^{i\varepsilon}$; ψ can be interpreted as the phase of the tractions at $r = L$ assuming that (1) still holds at this distance ahead of the crack tip. Y is a dimensionless geometric factor. Thus the calibration of a crack geometry is reduced to determining Y and ψ for a range of crack length-to-width ratios, properties of the material pair and load combinations. Dundurs (1968) has shown that the solution for a traction-prescribed interface crack problem depends only on two dimensionless material parameters, α and β, defined by

$$\alpha = \frac{\Gamma(\kappa_2+1)-(\kappa_1+1)}{\Gamma(\kappa_2+1)+(\kappa_1+1)}, \quad \beta = \frac{\Gamma(\kappa_2-1)-(\kappa_1-1)}{\Gamma(\kappa_2+1)+(\kappa_1+1)} \tag{5}$$

where $\Gamma = \mu_1/\mu_2$. So Y and ψ in (4) depend on material properties only through α and β.

3.2. *Variation of phase angle with distance*

The normal and shear tractions ahead of the crack tip are given by (3). When $\varepsilon \neq 0$ we cannot define a mode 1 and mode 2 stress intensity factor analogous to K_I and K_{II} used in the fracture mechanics of a homogeneous material. For $\varepsilon \neq 0$ the ratio of normal to shear tractions ahead of the crack, given by ψ_r, is no longer constant. It can be seen from (3) that $\psi_{r_2} = \psi_{r_1} + \varepsilon \ln (r_2/r_1)$ when distance changes from r_1 to r_2. Therefore the phase change $\Delta\psi$ as predicted by the K field is

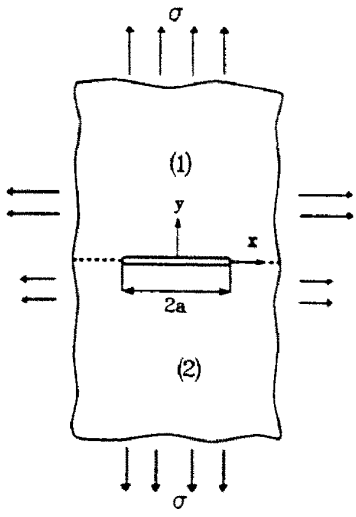

Fig. 3. Infinite plate with crack subjected to remote tension.

$$\Delta\psi = \psi_{r_2} - \psi_{r_1} = \varepsilon \ln\left(\frac{r_2}{r_1}\right). \tag{6}$$

The variation of phase angle over large distances can be significant even when ε is small.

To illustrate this point we consider the geometry shown in Fig. 3.. A finite crack of length $2a$ lies on an interface between two materials subjected to remote normal stress, σ at infinity. (Note that continuity of strains across the bond line requires that the normal stress parallel to the bond line be discontinuous.) A more general version of this problem is solved in Rice and Sih (1965). The full field normal and shear tractions ahead of the right crack tip are

$$\sigma_{yy}|_{\theta=0} = \frac{\sigma}{\sqrt{x^2-a^2}}\left[x\cos\left\{\varepsilon\ln\left(\frac{x+a}{x-a}\right)\right\} + 2a\varepsilon\sin\left\{\varepsilon\ln\left(\frac{x+a}{x-a}\right)\right\}\right]$$
$$\sigma_{xy}|_{\theta=0} = \frac{\sigma}{\sqrt{x^2-a^2}}\left[2a\varepsilon\cos\left\{\varepsilon\ln\left(\frac{x+a}{x-a}\right)\right\} + x\sin\left\{\varepsilon\ln\left(\frac{x+a}{x-a}\right)\right\}\right] \tag{7}$$

where x measures distance from the center of the plate. The phase angle ψ_r is defined as $\tan\psi_r = (\sigma_{xy}/\sigma_{yy})_{\theta=0}$. Figure 4 shows the variation of phase angle (in degrees) with distance

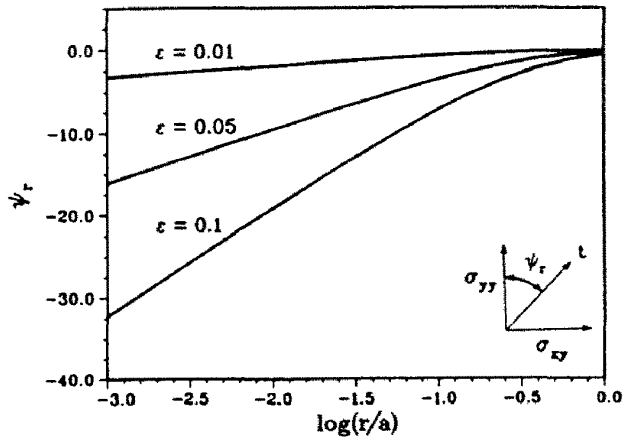

Fig. 4. Variation of phase angle with distance for crack in infinite plate for three values of ε.

from the crack tip given by the stresses in (7) for $\varepsilon = 0.01$, 0.05 and 0.1. These values of ε correspond to material moduli typical of a metal/metal, a metal/ceramic and an epoxy/ceramic interface respectively, under plane stress conditions.

We can see that the phase shift due to ε is quite a strong effect. When $\varepsilon = 0.05$ the phase shift over two decades of distance is about 11° and for $\varepsilon = 0.1$ it is about 25°. On a plot of $\log(r/a)$ the phase shift predicted by the K field (6) is a straight line. It can be seen that the variation of ψ_r based on (7) is essentially linear for $\log(r/a) < -1$. Though not shown, the phase shift given by the K solution closely matches the linear portion of the curves in Fig. 4. The change of phase angle with distance may be characterized using the phase index ε^*, defined by $\varepsilon^* \equiv (180/\pi)\varepsilon \ln 10$, which has the interpretation of the phase change in degrees over a decade increase in distance.

3.3. *Mode mixity and toughness surface*

There is ample experimental evidence that interfacial fracture toughness depends on mode mixity. Since phase angle depends on distance from the crack tip, an unambiguous specification of mode mixity for an interface crack is required.

When $\varepsilon = 0$, the mode mixity is fully specified by

$$\tan\psi = \left(\frac{\sigma_{xy}}{\sigma_{yy}}\right)_{\theta=0}, \quad \text{as } r \to 0. \tag{8}$$

An equivalent definition in terms of the classical stress intensity factors K_I and K_{II} is

$$\tan\psi = \frac{K_{II}}{K_I}. \tag{9}$$

The mode mixity concept can be extended to oscillatory fields by defining

$$\tan\tilde{\psi} = \left(\frac{\sigma_{xy}}{\sigma_{yy}}\right)_{\theta=0,\, r=\hat{L}} \tag{10}$$

or in terms of the complex stress intensity factor K

$$\tan\tilde{\psi} = \frac{\mathrm{Im}\{K\hat{L}^{i\varepsilon}\}}{\mathrm{Re}\{K\hat{L}^{i\varepsilon}\}}. \tag{11}$$

Here it is necessary to introduce a fixed length $\hat{L}$ in order that the mode mixity be specified unambiguously. $\hat{L}$ must be independent of the overall specimen size and specimen types; a sensible choice of $\hat{L}$ should fall between the inelastic zone size and the specimen size. For example, $\hat{L} = 100$ μm is suitable for many brittle bimaterial specimens at the laboratory scale. $\tilde{\psi}$ is calculated from ψ the phase of $KL^{i\varepsilon}$ using (6):

$$\tilde{\psi} = \psi + \varepsilon \ln(\hat{L}/L). \tag{12}$$

The mixed mode fracture condition is then

$$\mathcal{G}(\tilde{\psi}) = \mathcal{G}_c(\tilde{\psi}) \tag{13}$$

where $\mathcal{G}$ is the energy release rate given by

$$\mathcal{G} = \frac{1-\beta^2}{E^*}|K|^2 \tag{14}$$

where

$$\frac{1}{E^*} = \frac{1}{2}\left(\frac{1}{E_1'} + \frac{1}{E_2'}\right). \tag{15}$$

$E' = E/(1-\nu^2)$ for plane strain and $E' = E$ for plane stress.

Thus fracture resistance is unambiguously specified by a curve $\mathscr{G}_c(\tilde{\psi})$, together with a length $\tilde{L}$ for the definition of $\tilde{\psi}$. This engineering approach to quantifying the interfacial fracture resistance is an extension of the existing theory for homogeneous isotropic solids. The conceptual basis for this approach is summarized in Rice (1988) and several articles in a volume edited by Rühle *et al.* (1990). The experimental implementation can be found in Wang and Suo (1990), Liechti and Chai (in press) and Ahmad and Majumdar (unpublished).

3.4. *Near tip contact*

The displacement jumps across the crack face are given by

$$\delta_y + i\delta_x = \frac{8|K|}{E^* \cosh \pi\varepsilon \sqrt{1+4\varepsilon^2}} \sqrt{\frac{r}{2\pi}} e^{i(\psi - \gamma + \varepsilon \ln(r/L))} \tag{16}$$

where $\gamma = \tan^{-1} 2\varepsilon$. r is the distance along the crack face measured from the crack tip. This solution predicts contact between the crack faces (i.e. $\delta_y < 0$) for all values of ψ when $\varepsilon \neq 0$. The K solution is not valid within the zone of contact. Nevertheless, for a range of ψ this region is confined to a distance from the crack tip that is smaller than physically relevant size scales and within this range of ψ, K can still be used to characterize the crack tip field. A crack is defined as being open if

$$\delta_y \geqslant 0 \quad \text{for} \quad r_c \leqslant r \leqslant L \tag{17}$$

and $r_c \ll L$ (Rice, 1988; Shih and Asaro, 1989). r_c is thus the largest r for which the opening gap δ_y is negative. From (16) we see that for $\varepsilon > 0$

$$r_c/L = \exp\left[-(\pi/2 + \psi - \gamma)/\varepsilon\right]. \tag{18}$$

Rice (1988) suggests the requirement that $r_c/L < 0.01$. From (17) and (18) this implies that for $\varepsilon > 0$ the crack tip state may be characterized by the K field when

$$-\pi/2 + 6.6\varepsilon < \psi < \pi/2 + 2\varepsilon \tag{19}$$

(making the approximation that $\tan^{-1} 2\varepsilon = 2\varepsilon$). For $\varepsilon < 0$ the open crack range is

$$-\pi/2 + 2\varepsilon < \psi < \pi/2 + 6.6\varepsilon. \tag{20}$$

A similar expression for the range of ψ for an open crack has been provided in Wang and Suo (1990). This is a conservative estimate as discussed in a recent work by Yang and Shih (unpublished).

The specimens analyzed in this paper are calibrated for $|\psi| < 120°$ (see Fig. 9 for example). Equations (19) or (20) predict a closed crack for large negative and positive phase angles. Therefore at these phase angles the interpretation of test data using K may be questionable. In the above argument we have assumed that the crack faces are perfectly smooth. In practice there will be asperities on the crack faces so contact may occur even if $\delta_y \geqslant 0$.

3.5. K *Dominance*

We next address the subject of K dominance, i.e. the existence of a region within which the stresses are well approximated by the bimaterial K field.

It is assumed that close to the crack tip there is a region where non-linear effects dominate or where crack tip contact may occur, as discussed in the previous section. In order for K to characterize the fields we require the existence of an annular region $r_{pz} < r < L$ where the fields are well approximated by the K solution. r_{pz} is the larger of the plastic or contact zone sizes. A more complete discussion of the size requirements for the existence of a K dominant region is provided in a review article by Shih (in press).

The question of K dominance is addressed by comparing the full field stresses with the K field given in (1), scaled by the appropriate K value. We first consider the geometry shown in Fig. 3. The characteristic length for this geometry $L = 2a$. The stress intensity factor at the right hand tip is

$$\mathrm{Re}\,\{KL^{i\varepsilon}\} = \sigma\sqrt{\pi a}, \quad \mathrm{Im}\,\{KL^{i\varepsilon}\} = 2\varepsilon\sigma\sqrt{\pi a}. \tag{21}$$

In the form (4) we get $T = \sigma$, $Y = \sqrt{(1+4\varepsilon^2)\pi/2}$ and $\psi = \tan^{-1} 2\varepsilon$.

Figure 5a shows the comparison of the full field stresses given by (7) with the K solution given by (3) for $\varepsilon = 0.05$. The K field stresses are indicated by the open circles and triangles; the full field solution is given by the solid and broken lines. Note that the shear stress becomes negative close to the crack tip. This is a manifestation of the phase variation with distance discussed in Section 3.2. Good agreement between the K field and the full field solution is seen up to about $r/a = 0.2$. For this geometry and applied load, the predicted contact zone is many orders of magnitude smaller than the crack length. If in addition the zone where non-linear effects are important is also small compared to the crack length, then K dominance holds for this geometry.

To investigate K dominance in the finite-sized specimens calibrated in the paper, we compare numerically generated full field stresses with the K field. The computational model used is discussed in Section 4.1. For each specimen we consider the case when $\alpha = -0.5$ and $\beta = -0.125$ ($\varepsilon = 0.04$). The crack length to specimen width a/W is 0.3 in all cases. For

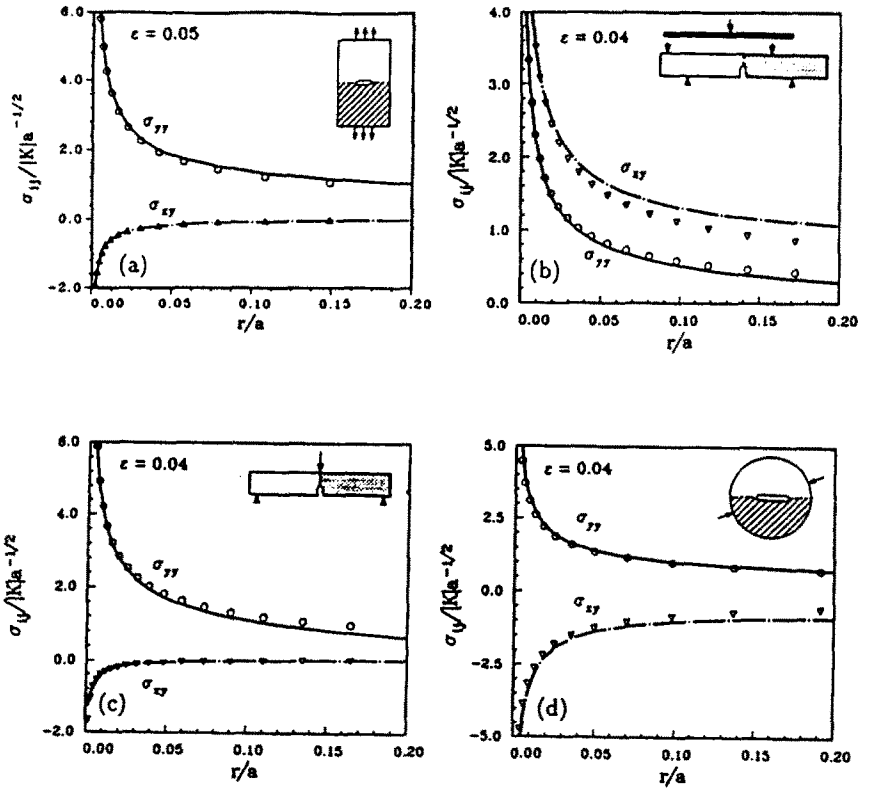

Fig. 5. Comparison of K field with full field solution. (a) Infinite plate with crack, (b) asymmetric bend specimen, (c) three-point bend specimen, (d) Brazilian disk.

the four-point bend configuration the relative offset s/W is 0.1 giving $\psi \approx 65°$. For the Brazilian disk the compression angle θ is 7.5° giving $\psi \approx -45°$ at the right hand tip. For the three-point bend specimen $\psi \approx 3°$. Figure 5b–5d shows the normal and shear stress ahead of the crack for the asymmetric four-point bend specimen, the three-point bend bar and the Brazilian disk. Again the K field solution is indicated on the plots by the open circles and triangles. We see that in all cases the K field is in good agreement with the full field solution over a significant fraction (about one tenth) of the crack length. Similar agreement is seen for all material combinations and crack geometries investigated. So provided the condition for an open crack, i.e. (19) or (20), is fulfilled and the zone of non-linear effects is small, a region of K dominance will exist for each specimen. Remarkably, the K dominant zone can extend to as much as one fifth of the ligament, e.g. Fig. 5a, c and d.

4. SPECIMEN CALIBRATION

4.1. *Computational model*

A finite element model is used to solve the elastic boundary value problem. The model employs 4 noded quadrilateral elements. Figure 6a shows the finite element mesh used to model the bend bar (four-point and three-point configurations) with crack length to width ratio a/W of 0.3. A typical mesh of the specimen has about 700 elements and 800 nodes. Figure 6b shows the mesh used to model the Brazilian disk specimen. A typical mesh contains about 1100 elements, and 1200 nodes. The crack tip is surrounded by an arrangement of wedge-shaped 4-noded elements. The nodes at the crack tip are constrained to have the same displacement which gives a good representation of the K singularity. The near tip mesh is shown in Fig. 6c. Different elastic properties are assigned to regions modeling materials 1 and 2. For the bend bars $B/W = 3$ in all cases and for the asymmetric bend bar $A/W = 2/3$. To extract the phase of K the interaction energy method of Shih and Asaro (1988) is used. A description of this method is provided in the Appendix. The path-independent integrals $\mathcal{G}_{int}$ and $\mathcal{G}$ used in evaluating Y and ψ are calculated using the domain

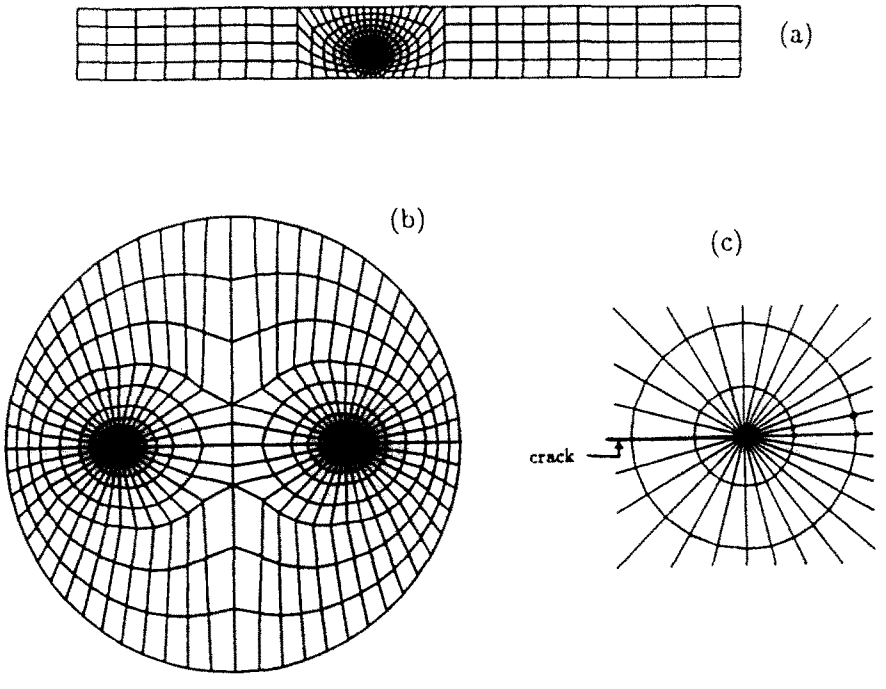

Fig. 6. Finite element meshes used. (a) Bend bar, (b) Brazilian disk, (c) near tip mesh.

integral method (Moran and Shih, 1987). For every solution 20 or more domains were used and the difference between the values extracted from the different domains is less than 1%.

4.2. *Material parameters*

The specimens have been calibrated for a range of α and for two values of β, $\beta = \alpha/3$ and $\alpha/4$. This corresponds to considering a range of E_2/E_1 and holding ν_1 and ν_2 fixed at 1/3. $\beta = \alpha/4$ corresponds to a plane strain assumption and $\beta = \alpha/3$ a plane stress assumption. The values of α chosen are $\alpha = -0.9$, -0.75, -0.5 and -0.25, which correspond to $E_2/E_1 = 19$, 7, 3 and 1.667 respectively. ε ranges from 0.002 to 0.1. This range includes most material combinations of interest. We have also included for comparison the calibration for a homogeneous material, $\alpha = \beta = 0$.

We should emphasize that for a given value of α and β, the K solution applies to both plane strain and plane stress specimens. However α and β correspond to different values of Young's modulus and Poisson's ratio depending on whether plane stress or plane stress conditions apply.

4.3. *Calibration of four-point bend specimens*

The generic form of K given in (4) for the bend bar geometry is

$$K = YT\sqrt{a}a^{-i\varepsilon}\, e^{i\psi} \tag{22}$$

where a is the crack length. Guided by the expression for a finite crack lying on an interface between two dissimilar materials we write K in the form

$$\begin{aligned} \text{Re}\,\{Ka^{i\varepsilon}\} &= \{\sigma f_1(a/W, \alpha, \beta) - 2\varepsilon\tau g_1(a/W, \alpha, \beta)\}\sqrt{a} \\ \text{Im}\,\{Ka^{i\varepsilon}\} &= \{\tau f_2(a/W, \alpha, \beta) + 2\varepsilon\sigma g_2(a/W, \alpha, \beta)\}\sqrt{a}. \end{aligned} \tag{23}$$

σ and τ are the nominal tensile and shear stresses along the crack plane and a/W is the ratio of crack length to specimen width. This form can be confirmed using dimensional analysis and linearity. Note that the four functions f_1, f_2, g_1 and g_2 are symmetric with respect to α and β, i.e $f(-\alpha, -\beta) = f(\alpha, b)$ where f is any of the four functions, f_1, f_2, g_1 or g_2. Changing the sign of α and β corresponds to interchanging materials 1 and 2.

4.3.1. *Symmetric configuration.* The symmetric four-point bend configuration, shown in Fig. 1a, is used to obtain phase angles close to zero. The normal and shear stresses ahead of the crack are given by

$$\sigma = P\left[\frac{3B}{2W^2}\right] \quad \text{and} \quad \tau = 0 \tag{24}$$

where P is the applied load per unit thickness. Substituting into (23) we get

$$\text{Re}\,\{Ka^{i\varepsilon}\} = P\left[\frac{3B}{2W^2}\right] f_1\sqrt{a}, \quad \text{Im}\,\{Ka^{i\varepsilon}\} = P\left[\frac{3B}{2W^2}\right] 2\varepsilon g_2\sqrt{a}. \tag{25}$$

We can recast these expressions for K in the form of (22) by writing

$$T = \sigma = P\left[\frac{3B}{2W^2}\right], \quad Y = \sqrt{f_1^2 + (2\varepsilon g_2)^2}, \quad \psi = \tan^{-1}\left\{\frac{2\varepsilon g_2}{f_1}\right\}. \tag{26}$$

4.3.2. *Asymmetric configuration.* For the asymmetric bend configuration the stresses on the crack plane are given by

$$\tau = -\frac{Q}{W}, \quad \sigma = -\frac{6Qs}{W^2} = 6\tau\frac{s}{W} \tag{27}$$

where $Q = -P(B-A)/(B+A)$ is the shear force per unit thickness and s is the load offset. (Note that Q is negative so σ and τ are both positive.) Substituting the expressions for σ and τ into (23) we get

$$\begin{aligned} \text{Re}\{Ka^{i\varepsilon}\} &= \frac{P}{W}\left[\frac{B-A}{B+A}\right]\{(6s/W)f_1 - 2\varepsilon g_1\}\sqrt{a}, \\ \text{Im}\{Ka^{i\varepsilon}\} &= \frac{P}{W}\left[\frac{B-A}{B+A}\right]\{f_2 + (12s/W)\varepsilon g_2\}\sqrt{a}. \end{aligned} \tag{28}$$

The advantage of this form for K is that the dependence on s/W is given explicitly. The functions f_1 and g_2 are the same as in (26). Again combining these two equations to give the form of K in (22) we get

$$T = \frac{P}{W}\left[\frac{B-A}{B+A}\right], \quad Y = \sqrt{Y_1^2 + Y_2^2}, \quad \psi = \tan^{-1}\left\{\frac{Y_2}{Y_1}\right\} \tag{29}$$

where

$$Y_1 = (6s/W)f_1 - 2\varepsilon g_1, \quad Y_2 = f_2 + (12s/W)\varepsilon g_2. \tag{30}$$

To achieve negative phase angles the positions of both loading and support points are interchanged. (To ensure an opening moment at the crack tip the load is applied to the right of the crack line with respect to the orientation of Fig. 1b.) T, Y and ψ are again given by (29) with

$$Y_1 = (6s/W)f_1 + 2\varepsilon g_1, \quad Y_2 = -f_2 + (12s/W)\varepsilon g_2. \tag{31}$$

Therefore to calibrate the four-point bend specimen fully we need only find the four functions, f_1, f_2, g_1 and g_2. These can be obtained by solving two boundary value problems —using the symmetric configuration we can obtain f_1 and g_2 directly using (25), and similarly using (28) with $s = 0$ we can obtain f_2 and g_1.

The functions f_1, f_2, g_1 and g_2 are plotted in Fig. 7a–h for the material combinations considered. We see that f_1 and g_1 are almost independent of α and β over the range of values chosen. f_2 and g_2 show stronger dependence on α and β. Note that the calibration functions for the four-point bend bar are independent of the ratios A/W and B/W.

As shown earlier we can calculate Y and ψ for each geometry from these four functions. Figure 8a–d gives Y and ψ versus a/W for the symmetric configuration for the full range of α and β considered. Y depends very weakly on α and β; however, ψ has a strong dependence on α and β. Figure 9 gives Y and ψ for asymmetric configuration for various a/W ratios with $\alpha = -0.75$, $\beta = \alpha/4$. Figure 9a and b is for the "positive" set-up shown in Fig. 1b and Fig. 9c, d is for the "negative" set-up. The horizontal dotted line in Fig. 9b, d indicates the range of ψ for which we have an open crack as discussed in Section 3.4. For this material combination, $\varepsilon = 0.06$ so from (19) the crack is open in the range $-67° < \psi < 97°$.

A similar calibration for a homogeneous material, requiring only two functions, f_1 and f_2, has been given in Suresh *et al.* (1990). However, the sign of the phase angle ϕ (which is equivalent to our ψ) should be switched. This does not affect the results presented therein as the fracture toughness curve for a homogeneous material is symmetric, i.e. $K_c(-\phi) = K_c(\phi)$.

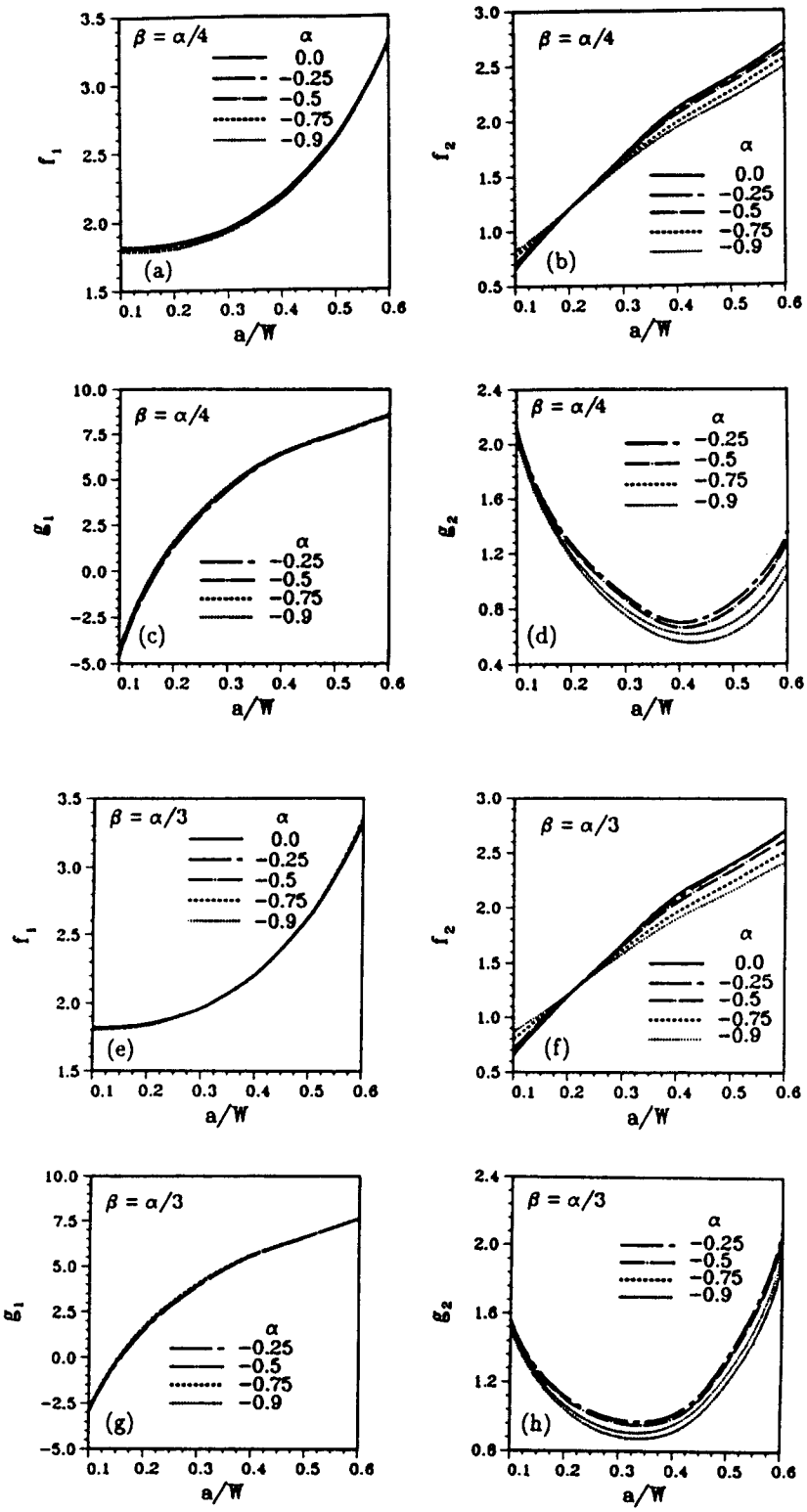

Fig. 7. Plot of functions f_1, f_2, g_1, g_2 versus a/W for four-point bend specimen over a range of α: (a)–(d) $\beta = \alpha/4$, (e)–(h) $\beta = \alpha/3$.

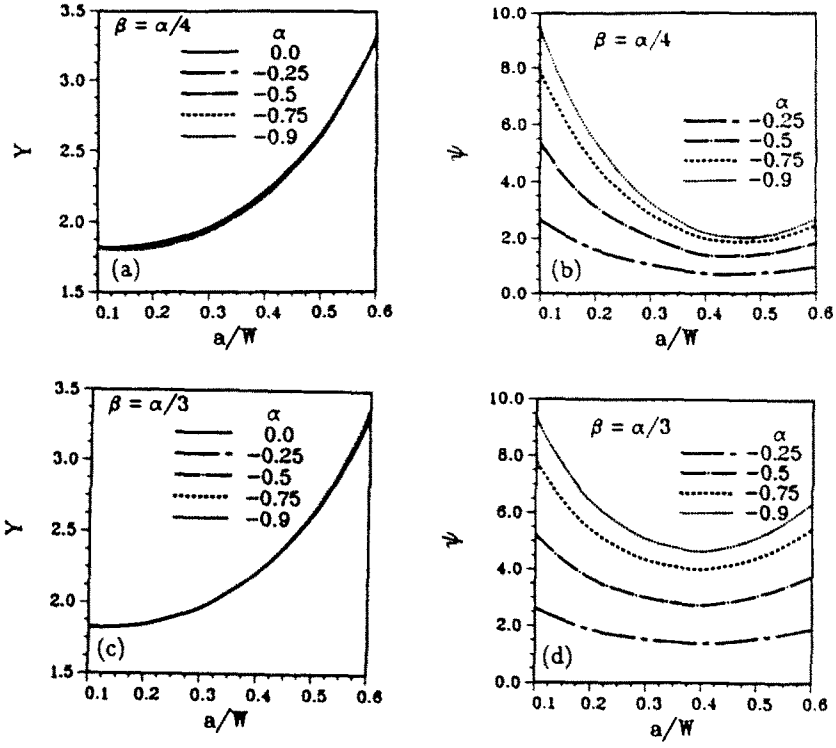

Fig. 8. Plot of Y and ψ versus a/W for symmetric bend specimen for a range of α. (a) and (b) $\beta = \alpha/4$, (c) and (d) $\beta = \alpha/3$.

4.4. *Three-point bend specimen*

The form of (23) could be utilized in calibrating the three-point bend specimen. However, for the three-point bend specimen there is an undetermined shear force acting along the interface. The calibration therefore depends additionally on the loading through the ratio B/W. We therefore provide Y and ψ directly via

$$K = YT\sqrt{a}a^{-i\varepsilon}e^{i\psi} \tag{32}$$

where Y and ψ are understood to depend on B/W and a/W. In this case $T = P(3B/W^2)$. If materials 1 and 2 are switched Y remains the same but the sign of ψ is switched.

Figure 10a–d shows Y and ψ versus a/W for the three-point bend over the range of α with $\beta = \alpha/3$ and $\alpha/4$ as before. The functions given are for $B/W = 3$. The features are similar to that seen earlier for the symmetric four-point bend configuration. The dependence on B/W is weak. If B/W is increased by a factor of 3, Y increases by 4% and ψ decreases by about 2°.

4.5. *Brazilian disk*

The form of (23) is not applicable to the Brazilian disk specimen. We write K once again in the form of (4) as

$$K = YT\sqrt{2a}(2a)^{-i\varepsilon}e^{i\psi} \tag{33}$$

where a is the half crack length. For the disk $T = P/2W$ where W is the radius of the disk. Note that the dependence of Y and ψ on compression angle θ is not known explicitly. Furthermore the stress intensity factors at the two crack tips will not be the same, so Y and

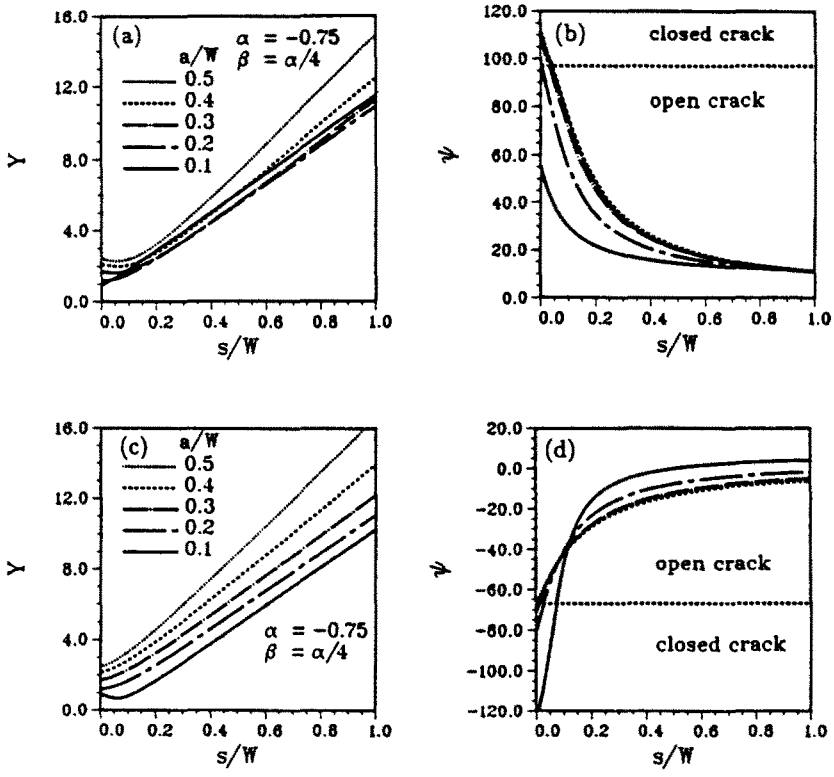

Fig. 9. Plot of Y and ψ versus s/W for asymmetric bend specimen for $\alpha = -0.75$, $\beta = \alpha/4$. (a) and (b) "positive" set-up, (c) and (d) "negative" set-up.

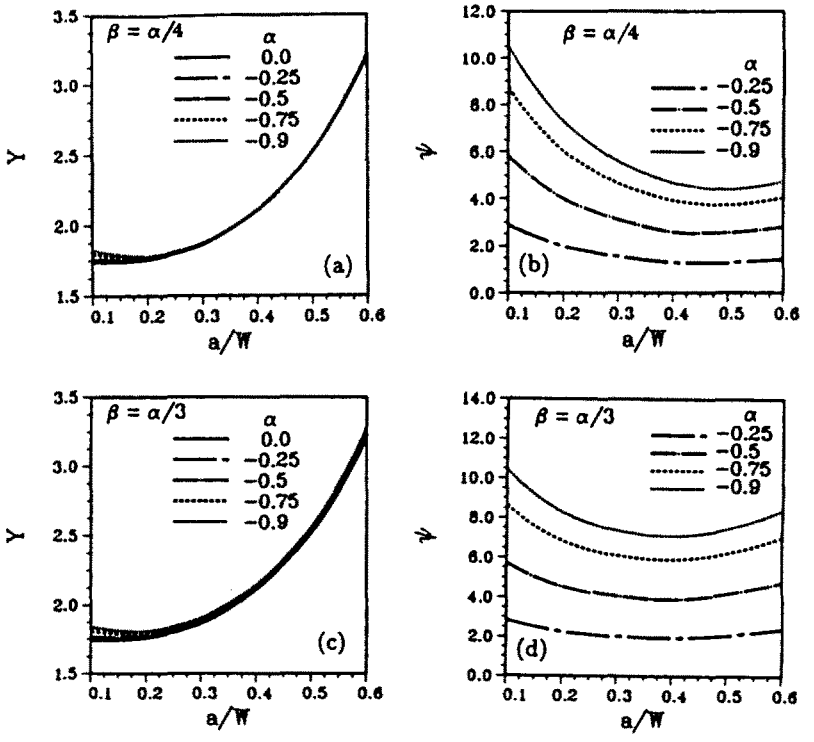

Fig. 10. Plot of Y and ψ versus a/W for three-point bend specimen for a range of α. (a) and (b) $\beta = \alpha/4$, (c) and (d) $\beta = \alpha/3$.

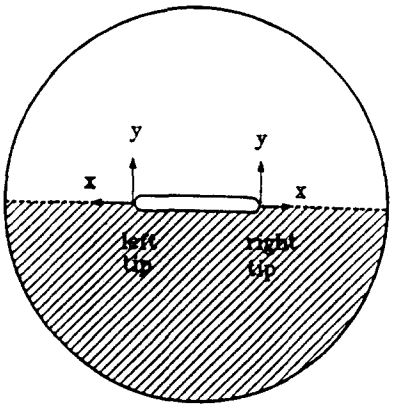

Fig. 11. Convention used in definition of phase angle at left and right tip for Brazilian disk.

ψ must be provided for each tip. The coordinate system used in the definition of ψ at the right and left tip is shown in Fig. 11.

In Figs 12 and 13 we have plotted Y and ψ at the left and right tip for $a/W = 0.3$ and 0.5, respectively. The compression angle θ ranges from 0 to 30°. Y_{right} and Y_{left} are the amplitudes at the right and left tip, and ψ_{right} and ψ_{left} are the phase angles at the right and left tip. For negative compression angles Y and ψ for the left and right tips are switched, i.e. $Y_{right}(-\theta) = Y_{left}(\theta)$, $\psi_{right}(-\theta) = \psi_{left}(\theta)$ and vice versa. If materials 1 and 2 are switched Y and ψ at the two tips are interchanged and also the sign of ψ is changed, i.e. $Y_{right}(-\alpha, -\beta) = Y_{left}(\alpha, \beta)$, and $\psi_{right}(-\alpha, -\beta) = -\psi_{left}(\alpha, \beta)$ and vice versa.

4.6. *Calibration for residual stresses*

The fabrication of a bimaterial specimen often involves large temperature changes in the specimen. For example diffusion bonding at elevated temperatures is commonly used to join the two materials. This can give rise to large residual stresses after cooling due to the difference in the thermal expansion coefficients of the two materials. These residual stresses produce a stress intensity factor which contributes to the resultant K.

As an example we calculate K due to residual stresses in the bend bar geometry shown in Fig. 1. The thermal stress problem can be solved using Eshelby's cut and paste (superposition) procedure. With no loss of generality we assume that $\alpha_1 > \alpha_2$, where α_1 and α_2 are the thermal expansion coefficients of materials 1 and 2.

The upper and lower materials are first considered to be separate. The upper material undergoes a stress-free uniform thermal contraction with $\epsilon_{11} = \Delta\alpha\Delta T$ where $\Delta\alpha = \alpha_1 - \alpha_2$, and ΔT is the temperature change. In order to maintain compatibility at the bimaterial interface a normal stress, $\sigma = \Delta\alpha\Delta T E_1/(1-\nu_1)$ (in plane strain) parallel to the interface is then applied. For this step $K = 0$ as the upper and lower halves are separate. The upper and lower materials are then welded together and the applied stress is removed by applying σ in the opposite sense. K due to the residual stress is thus found by solving the boundary value problem shown in Fig. 14. (For $\alpha = \beta = 0$ this produces a pure Mode II field at the crack tip.)

Y and ψ are plotted in Fig. 15a-d for the material combinations considered. $T = \Delta\alpha\Delta T E_1/(1-\nu_1)$ for plane strain. For plane stress $T = \Delta\alpha\Delta T E_1$ ($L = a$ as before). K obtained from the thermal analysis is then superimposed on the K value obtained for the experiment.

It should be noted that the above analysis does not allow for thermal relaxation of stresses at high temperatures, as would be encountered under diffusion bonding conditions. When relaxation of stresses occurs our analysis overestimates the K due to residual stresses.

5. DISCUSSION

We have calibrated two types of specimen which can be used to measure interfacial fracture toughness as a function of mode mixity. Heretofore sandwich specimens have

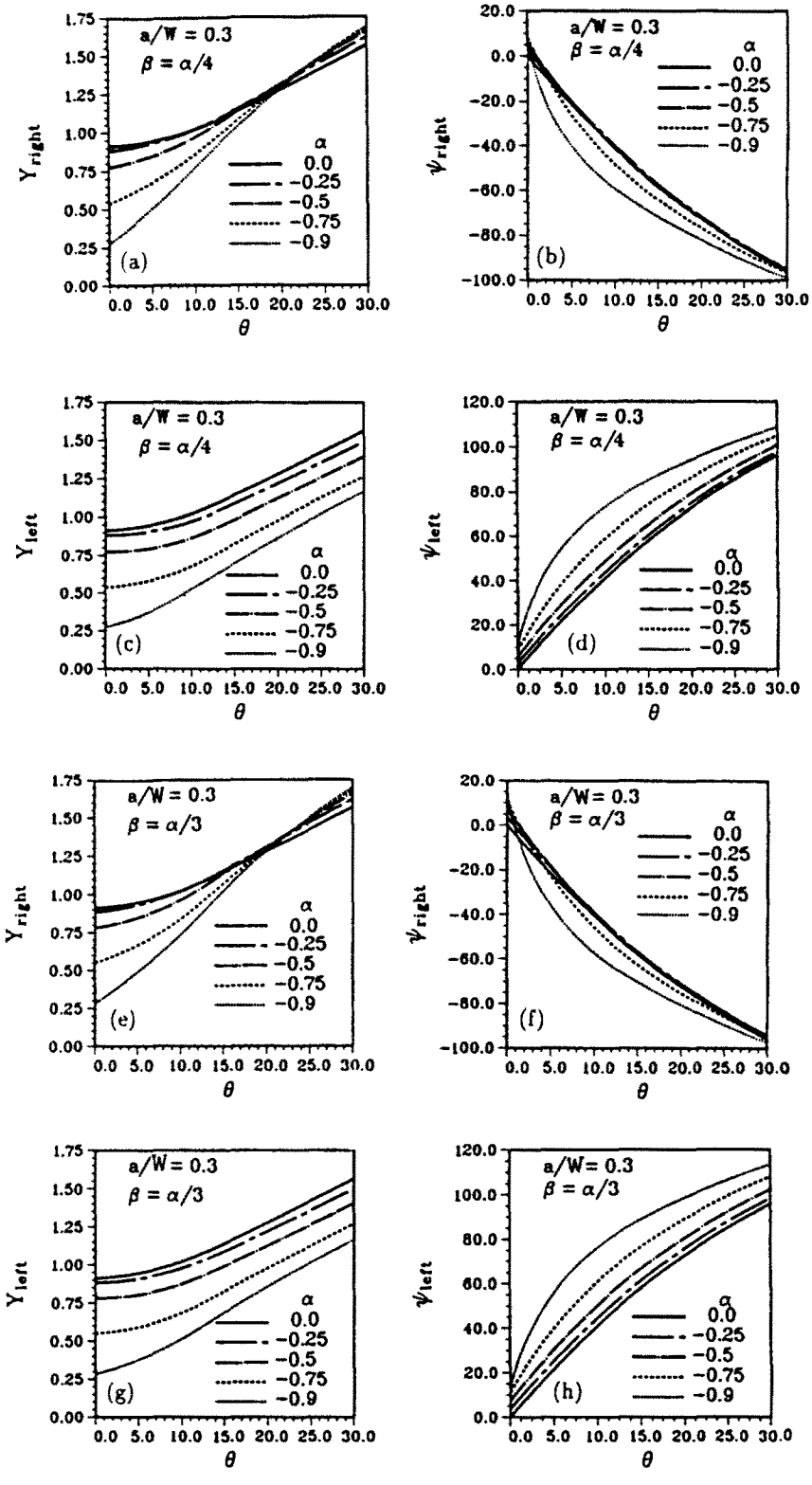

Fig. 12. Plot of Y and ψ versus θ for Brazilian disk specimen with $a/W = 0.3$ over a range of α; (a)–(d) $\beta = \alpha/4$, (e)–(h) $\beta = \alpha/3$.

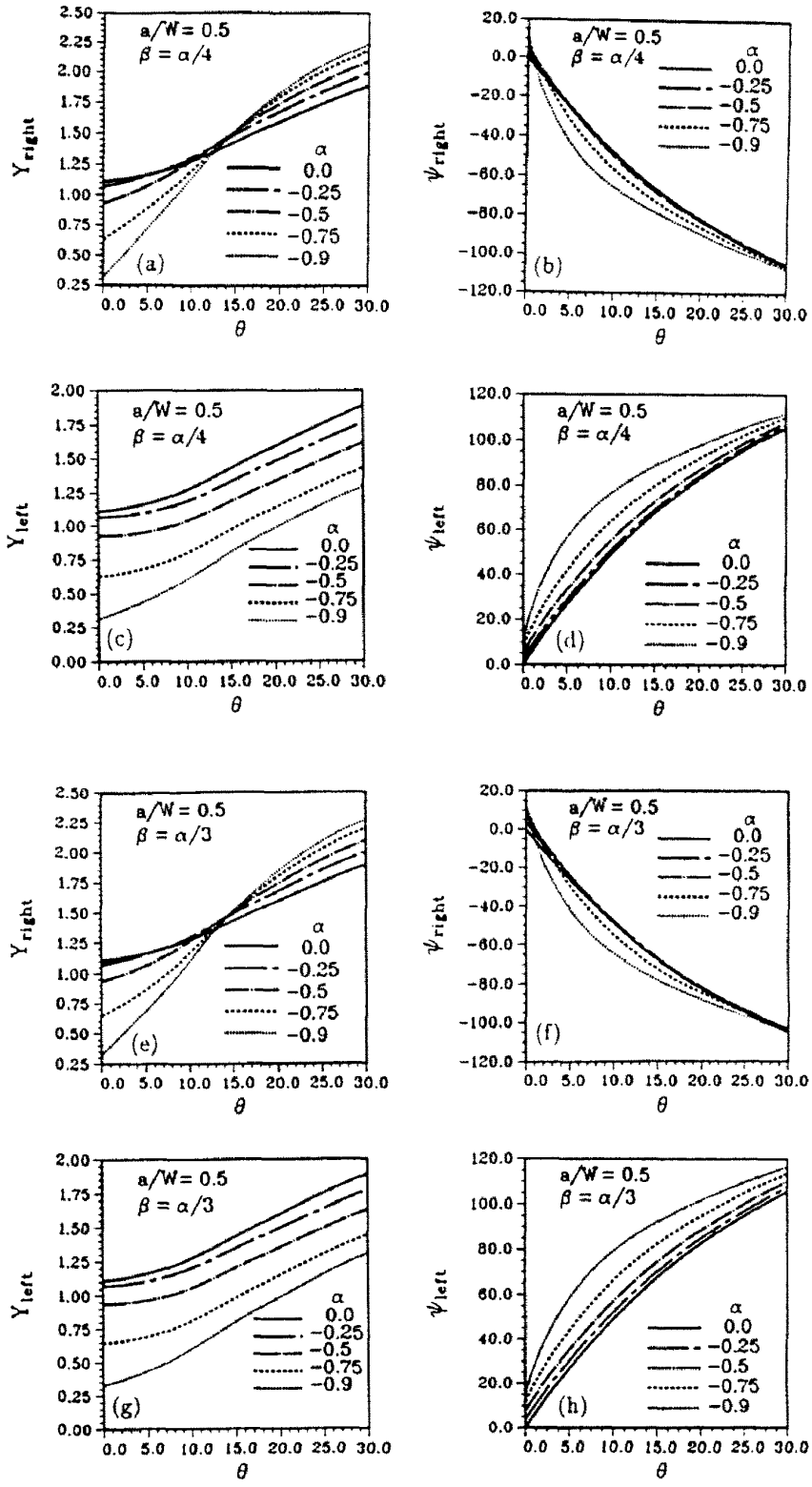

Fig. 13. Plot of Y and ψ versus θ for Brazilian disk specimen with $a/W = 0.5$ over a range of α; (a)–(d) $\beta = \alpha/4$, (e)–(h) $\beta = \alpha/3$.

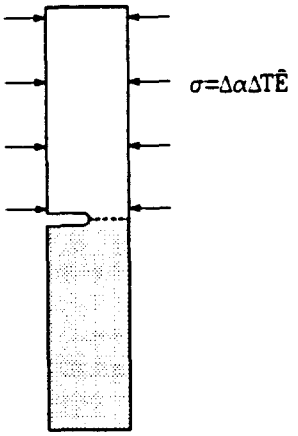

Fig. 14. Boundary value problem solved to find K due to residual stress in bend bar. $\hat{E} = E_1/(1-\nu_1)$ in plane strain; E_1 in plane stress.

primarily been used to measure interfacial toughness. These specimens have the advantage that the residual stress in the layer does not affect the stress intensity factor and can be ignored when evaluating interfacial toughness. Also these specimens can be calibrated easily in terms of the stress intensity factor for a homogeneous specimen of the bulk material (Suo and Hutchinson, 1989). However a crack in a sandwich specimen may kink out of the interface under certain conditions and grow in the interlayer (Wang and Suo, 1990) in which case a valid interfacial toughness measurement is not obtained. Crack extension within the sandwiched layer does not arise in the specimens proposed in this paper.

With regard to the relative merits of the specimens calibrated here, the symmetric four-point bend specimen is preferred to the three-point bend specimen for measuring fracture

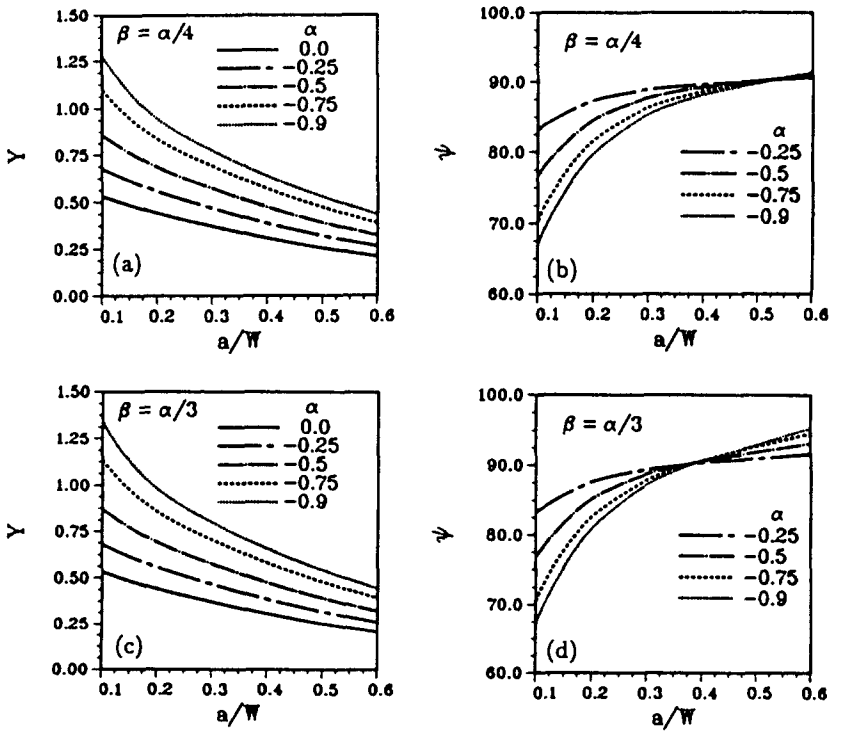

Fig. 15. Y and ψ versus a/W for K in bend bar due to residual thermal stress for a range of α; (a) and (b) $\beta = \alpha/4$, (c) and (d) $\beta = \alpha/3$.

toughness for phase angles close to zero. If the loading point is slightly off-center for the three-point bend specimen this will change the stress intensity factor at the crack tip. This is not the case for the four-point bend specimen as the bending moment is constant over most of the length of the specimen.

The full range of mode mixities can be obtained using the Brazilian disk specimen. This specimen is attractive because of the ease of loading of the specimen. However, introducing a crack in the disk may be difficult. Furthermore since the specimen has two crack tips it may be difficult to determine the tip at which fracture first initiates. This leads to some ambiguity in determining fracture toughness using this specimen. This difficulty does not arise with the bend bar which has a single crack tip. Distance measurements are also easier to make using a bend bar type geometry as one is measuring a linear distance, while with the disk specimen angular measurements are required which in general cannot be made with the same accuracy.

If a stiff material is bonded to a more compliant material local indentation may occur at the load points located in the softer material. For this reason it may be convenient to use test specimens in which the compliant layer is held between two layers of the stiffer material. This ensures that the load and support points are located in the stiffer material. Provided that the span of the intermediate layer is comparable to the specimen width W the calibration functions for this type of specimen are the same as those presented here. Calculations have been carried out for the bend bar specimen where the height of the intermediate layer was equal to the specimen width. The results obtained differed negligibly from those presented here.

Acknowledgements—N. P. O'Dowd and C. F. Shih are supported by the Office of Naval Research through ONR Grant N00014-90-J1380 and the Materials Research Laboratory at Brown University funded by the National Science Foundation, Grant DMR-8714665. M. Stout is supported by the Office of Basic Energy Sciences, Division of Materials Sciences, US Department of Energy. The computations were carried out at the Computational Mechanics Research Facility within the Division of Engineering of Brown University. Helpful discussions with Professor Zhigang Suo are gratefully acknowledged.

REFERENCES

Ahmad, J. and Majumdar, B. S. (unpublished). An engineering fracture mechanics analysis of metal/ceramic and ceramic/ceramic joints.

Atkinson, C., Smelser, R. E. and Sanchez, J. (1982). Combined mode fracture via the cracked Brazilian disk test. *Int. J. Fract.* **18**(4), 279–291.

Cao, H. C. and Evans, A. G. (1989). An experimental study of the fracture resistance of bimaterial interfaces. *Mech. Mater.* **7**, 295–305.

Charalambides, P. G., Lund, J., Evans, A. G. and McMeeking, R. M. (1989). A test specimen for determining the fracture resistance of a bimaterial interface. *J. Appl. Mech.* **56**, 77–82.

Dundurs, J. (1968). Elastic interaction of dislocations with inhomogeneities. In *Mathematics Theory of Dislocations*, pp. 70–115. American Society of Mechanical Engineering, New York.

Liechti, K. M. and Chai, Y-S. (In press). Biaxial loading experiments for determining interfacial fracture toughness. *J. Appl. Mech.*

Moran, B. and Shih, C. F. (1987). Crack tip and associated domain integrals from momentum and energy balance. *Engng Fract. Mech.* **27**(6), 615–642.

Rice, J. R. and Sih, G. C. (1965). Plane problems of cracks in dissimilar media. *J. Appl. Mech.* **32**, 418–423.

Rice, J. R. (1988). Elastic fracture mechanics concepts for interfacial cracks. *J. Appl. Mech.* **55**, 98–103.

Rice, J. R., Suo, Z. and Wang, J.-S. (1990). Mechanics and thermodynamics of brittle interfacial failure in bimaterial systems. In *Metal Ceramic Interfaces. Acta-Scripta Metallurgica Proceedings*, Vol. 4, pp. 269–294. Pergamon Press, New York.

Rühle, M., Evans, A. G., Ashby, M. F. and Hirth, J. P. (1990). *Metal Ceramic Interfaces. Acta-Scripta Metallurgica Proceedings*, Vol. 4. Pergamon Press, New York.

Shetty, D. K., Rosenfield, A. R. and Duckworth, W. H. (1987). Mixed-mode fracture in biaxial stress state: application of the diametral-compression (Brazilian disk) test. *Engng Fract. Mech.* **26**(6), 825–840.

Shih, C. F. (In press). Cracks on bimaterial interfaces: elasticity and plasticity aspects. *Mater. Sci. Engng.*

Shih, C. F. and Asaro, R. J. (1988). Elastic–plastic analysis of cracks on bimaterial interfaces: Part I—Small scale yielding. *J. Appl. Mech.* **55**, 299–316.

Shih, C. F. and Asaro, R. J. (1989). Elastic–plastic analysis of cracks on bimaterial interfaces: Part II—Structure of small-scale yielding fields. *J. Appl. Mech.* **56**, 763–779.

Stout, M. G., O'Dowd, N. P. and Shih, C. F. (Unpublished). Interfacial fracture toughness of niobium/alumina systems.

Suo, Z. and Hutchinson, J. W. (1989). Sandwich test specimens for measuring interface crack toughness. *Mater. Sci. Engng* **A107**, 135–143.

Suresh, S., Shih, C. F., Morrone, A. and O'Dowd, N. P. (1990). Mixed-mode fracture toughness of ceramic materials. *J. Am. Ceram. Soc.* **73**, 1257–1267.

Wang, J.-S. and Suo, Z. (1990). Experimental determination of interfacial toughness curves using Brazil-nut-sandwiches. *Acta Metall.* **38**(7), 1279–1290.
Yang, W. and Shih, C. F. (Unpublished). Fracture along an interlayer.

APPENDIX

A numerical method for extracting the real and imaginary part of K has been presented by Shih and Asaro (1989). The energy release rate for a crack lying on an interface between two isotropic elastic materials is

$$\mathcal{G} = \frac{1-\beta^2}{E^*}(K_1^2+K_2^2). \tag{A1}$$

The effective modulus E^* was defined in Section 3.3. K_1 and K_2 are the real and imaginary parts of K.

If we superimpose an auxiliary field of known intensity k_1 onto the actual field, the auxiliary field has energy release rate

$$\mathcal{G}_{aux} = \frac{1-\beta^2}{E^*}k_1^2 \tag{A2}$$

and the total energy release rate is

$$\mathcal{G}_{tot} = \frac{1-\beta^2}{E^*}[(K_1+k_1)^2+K_2^2]. \tag{A3}$$

We define the interaction energy release rate as

$$\mathcal{G}_{int} = \mathcal{G}_{tot}-(\mathcal{G}+\mathcal{G}_{aux}). \tag{A4}$$

Substituting into (A4) we get

$$\mathcal{G}_{int} = 2\left(\frac{1-\beta^2}{E^*}\right)K_1k_1.$$

Thus for an auxiliary field of known intensity factor, say $k_1 = 1$, we can extract the actual K_1 via

$$K_1 = \frac{1}{2}\left(\frac{E^*}{1-\beta^2}\right)\mathcal{G}_{int}. \tag{A5a}$$

Similarly K_2 is determined from

$$K_2 = \frac{1}{2}\left(\frac{E^*}{1-\beta^2}\right)\mathcal{G}_{int} \tag{A5b}$$

where $\mathcal{G}_{int}$ is the interaction energy associated with an auxiliary field of intensity, $k_2 = 1$.

The energy release rate $\mathcal{G}$ in linear elasticity is given by the path-independent J-integral:

$$\mathcal{G} = J = \int_\Gamma\left(\tfrac{1}{2}\sigma_{ik}\varepsilon_{ik}\delta_{1j}-\sigma_{ij}\frac{\partial u_i}{\partial x_1}\right)n_j\,d\Gamma \tag{A6}$$

where Γ is a contour beginning at the bottom crack face and ending at the top face, n_j is the outward unit normal to Γ and δ_{ij} is the Kronecker delta.

Using reciprocity and eqns (A4) and (A6) we write

$$\mathcal{G}_{int} = \int_\Gamma\left(\sigma_{ik}(\varepsilon_{ik})_{aux}\delta_{1j}-\sigma_{ij}\left(\frac{\partial u_i}{\partial x_1}\right)_{aux}-(\sigma_{ij})_{aux}\frac{\partial u_i}{\partial x_1}\right)n_j\,d\Gamma. \tag{A7}$$

$\mathcal{G}_{int}$ is also path-independent by virtue of the path-independence of (A6). The auxiliary fields $(\sigma_{ij})_{aux}$, $(\varepsilon_{ij})_{aux}$, $(\partial u_i/\partial x_1)_{aux}$ are known and the actual fields are obtained from the full field finite element analysis. Thus by evaluating the path-independent integral for $\mathcal{G}_{int}$ the magnitude and phase of K can be evaluated from (A5).